JGR Space Physics

RESEARCH ARTICLE
10.1029/2024JA033158

Energetic Electron Precipitation From the Radiation Belts: Geomagnetic and Solar Wind Proxies for Precipitation Flux Magnitudes

Malcolm Crack[1], Craig J. Rodger[1], Mark A. Clilverd[2], Aaron T. Hendry[1,2], and Jean-Andre Sauvaud[3]

[1]Physics Department, University of Otago, Dunedin, New Zealand, [2]British Antarctic Survey (UKRI-NERC), Cambridge, UK, [3]Institut de Recherche en Astrophysique et Planétologie (IRAP), Toulouse, France

Key Points:

- The suitability of geomagnetic and solar wind indices for use as proxies for energetic electron precipitation flux variations are examined
- For medium energy electron precipitation (i.e., >100 keV), the best proxies were found to be either the Ap or Dst geomagnetic indices
- For relativistic energy electron precipitation (i.e., >700 keV), the best proxies were identified as the Kp or AE geomagnetic indices

Supporting Information:

Supporting Information may be found in the online version of this article.

Correspondence to:

M. A. Clilverd,
macl@bas.ac.uk

Citation:

Crack, M., Rodger, C. J., Clilverd, M. A., Hendry, A. T., & Sauvaud, J.-A. (2025). Energetic electron precipitation from the radiation belts: Geomagnetic and solar wind proxies for precipitation flux magnitudes. *Journal of Geophysical Research: Space Physics*, *130*, e2024JA033158. https://doi.org/10.1029/2024JA033158

Received 7 AUG 2024
Accepted 10 FEB 2025

Abstract Previously the geomagnetic Ap index has been used as a proxy to produce empirical energetic electron precipitation (EEP) forcing representations suitable for incorporation into coupled-climate model runs. The long-running Ap index has the advantage that it allows descriptions of EEP to be made for periods outside the current satellite era, but its suitability has not been checked against other reasonable proxies. In this study three different satellite electron precipitation data sets (DEMETER, POES, and SAMPEX) are used to examine the suitability of a variety of geomagnetic and solar wind proxies to represent EEP flux in different energy ranges. Analysis was undertaken using indices at their fundamental timescales (typically minutes or hours). For medium energy electron precipitation (i.e., >100 keV), the best proxy is found to be either Ap or Dst. For relativistic energy electron precipitation (i.e., >700 keV), the best proxy is Kp or AE, the latter suggesting a connection to substorm activity. The identification of the Ap index as one of the best proxies for medium energy EEP supports the approach taken by van de Kamp et al. (2016), https://doi.org/10.1002/2015jd024212. An EEP forcing capability based on Ap was developed by those authors for inclusion as a solar forcing factor in the Coupled Model Intercomparison Project Phase 6 of the World Climate Research Program.

Plain Language Summary In order to determine the effect of energetic particle forcing on the Earth's atmosphere over decadal timespans it has been necessary to develop models of energetic electron precipitation (EEP) based on long time-series geomagnetic indices. This has been done using the geomagnetic index Ap which was recommended for use for EEP forcing in the Coupled Model Intercomparison Project Phase 6 of the World Climate Research Program. However, in that process Ap was not selected as a proxy for EEP based on its merit, but rather for convenience. Here we use the EEP measurements from three different satellite datasets, two individual spacecraft and 1 constellation. We look over a range of particle detector configurations to test for the "best" proxy; investigating both geomagnetic and solar wind parameters. In all we tested seven different indices to see how good they were as proxies for EEP and found that for medium energy electrons the best proxies were Ap, and Dst—both geomagnetic indices. For higher energies, relativistic electron precipitation is best proxied by Kp or AE. This should be considered if and when any solar forcing factors are expanded into these relativistic energies for EEP.

1. Introduction

Descriptions of solar forcing terms that are recommended for use in coupled-climate model runs have been summarized by Matthes et al. (2017). The forcing terms include solar irradiance, tropical ozone variations, and energetic particle precipitation. Particle precipitation is one of the routes by which the Sun can link to the climate system; energetic electrons and protons can change atmospheric chemistry through the production of reactive species in the upper atmosphere (Brasseur & Solomon, 2005). The Matthes et al. recommendations were published in order to facilitate the inclusion of solar forcing in the Coupled Model Intercomparison Project Phase 6 (CMIP-6) of the World Climate Research Program (WCRP). Due to observed polar chemical changes caused by energetic particle precipitation (e.g., Andersson et al., 2018 and references therein), the solar forcing terms for CMIP-6 now includes medium-high energy electron precipitation (EEP, ~10 keV–1 MeV). The recommended EEP model was developed by Van de Kamp et al. (2016) and uses the geomagnetic index Ap as a proxy to describe the variations of precipitating electron flux. The choice of Ap was more due to practicality rather than a carefully thought-out scientific decision, as techniques have been developed to extend the Ap index beyond its start date in 1932, and thus facilitate long time series analysis of climate model results to include periods from as

early as 1850 (Matthes et al., 2017). That timing was a requirement for model development to represent solar forcing inside this effort. Typically, for multi-year coupled-climate model runs Ap is provided as a daily mean value rather than its fundamental 3-hr time resolution.

However, other geomagnetic indices and solar wind parameters have been used as proxies to describe radiation belt flux variability. It is well known that the geomagnetic AE index can be used as a good proxy for substorm activity (e.g., Belakhovsky et al., 2023), and substorms are expected to trigger processes which lead to high EEP fluxes (Cresswell-Moorcock et al., 2013; Jaynes et al., 2015; Rodger et al., 2022). Nesse Tyssøy et al. (2021) combined the Medium Energy Proton and Electron Detectors (MEPED) instrument on board the NOAA/Polar Orbiting Environmental Satellites (POES) 0° and 90° telescope electron flux measurements, that is, the bounce-loss-cone (BLC) and quasi-trapped viewing directions and calculated daily mean values of electron precipitation fluxes. They concluded that there was a strong correlation between the daily resolved AE index and >43 keV electron precipitation fluxes. However, in that study AE was found to be a poor predictor for >292 keV electron fluxes. In contrast, Rodger et al. (2022) investigated how EEP varied during and after clusters of substorms, looking at the MEPED/POES 0° (BLC) telescope electron flux measurements. Rodger et al. undertook a superposed epoch analysis of 15 min resolution median EEP fluxes from 2005 to 2018 using a SOPHIE-generated substorm list (Forsyth et al., 2015). During and after substorm clusters there was a good correlation with AE magnitude for >30 keV and >300 keV electron fluxes, but only after careful consideration of the instrument noise-floor.

Current substorm mechanisms such as those described in Jaynes et al. (2015) suggest that VLF chorus waves play a significant role in electron precipitation characteristics, particularly as electrons drift toward the morning side after injection into the region of MLT midnight. The geomagnetic index Kp is often used as a proxy for VLF chorus variability, particularly lower band chorus (Agapitov et al., 2015; Shprits et al., 2007). Simms et al. (2018) analyzed the variations of trapped relativistic electron fluxes at geostationary orbit, concluding that ULF and VLF waves (particularly VLF chorus) were important factors in determining variability, and that solar wind inputs such as velocity, density, and orientation (Bz) had moderate influence as well.

In order to investigate the suitability of a range of geomagnetic indices and solar wind parameters to describe the variability of EEP, in this paper we undertake analysis of EEP measurements from three different satellites. This includes two separate spacecraft as well as a constellation made up of multiple near identical spacecraft. Inter-comparison between the somewhat disparate satellite observations is made within specific orbital confines where detector performances are similar, and over common energy ranges. Standard deviations between the observed electron precipitation fluxes and a range of geomagnetic and solar wind parameters are determined. Standard errors of those deviations are also calculated, providing a measure of the uncertainty in the results. From this analysis recommendations are made regarding the best parameter to use to capture the variability of EEP magnitudes.

2. Experimental Method

Comprehensive descriptions of EEP, in terms of flux measured over a range of energies, are complicated by the limitations of individual satellite measurements. The Detection of Electromagnetic Emissions Transmitted from Earthquake Regions (DEMETER) satellite carried one electron particle detector, but with high energy resolution from 70 keV–2.2 MeV (Sauvaud et al., 2006). MEPED/POES EEP measurements (Evans & Greer, 2006) have been made over a 20+ year period and have multiple detectors flying at any one time (Rodger et al., 2010a, 2010b, 2022). However, MEPED/POES EEP measurements are limited to three medium energy integral channels (30 keV–2.5 MeV), with a potential fourth (>700 keV) being included through the contamination of one of the proton channels (Peck et al., 2015; Yando et al., 2011). The Solar Anomalous and Magnetospheric Particle Explorer (SAMPEX) satellite carried one detector, designed to be sensitive to relativistic (>1.05 MeV) electron fluxes (Klecker et al., 1993; Nakamura et al., 1998). The three satellites measurements of energetic electron fluxes relevant to this study are detailed below.

2.1. DEMETER

DEMETER was launched into a Sun-synchronous orbit at ~710 km in June 2004. The mission ended in March 2011. DEMETER's Instrument for Detecting Particles (IDP) instrument measured mostly drift-loss-cone electrons from ~70 keV to ~2.2 MeV in 126 channels (although the upper and lower energy channels are not used).

The instrument has been described in detail by Sauvard et al. (2006). Our study uses IDP data from August 2004 to March 2011. For operational reasons the IDP instrument measurements were not routinely undertaken at latitudes >65° (Cussac et al., 2006), and thus there is a limited range of observations which can be used in our study. This limitation is discussed in more detail in subsection 2.4. The IDP instrument is capable of measuring BLC fluxes instead of DLC fluxes when the DEMETER satellite is overhead of the North Atlantic region (see discussions below). The time resolution of the flux measurements was 4 s.

2.2. POES

The POES satellites operate in a Sun-synchronous orbit at ~835 km. Our study includes both the NOAA POES satellites (NOAA-15 to NOAA-19), and the EUMetSat POES satellites (MetOp-1, and -2), all of which carry the SEM-2 instrument suite (Evans & Greer, 2006; https://www.ncei.noaa.gov/data/poes-metop-space-environment-monitor/doc//sem2_docs/2006/SEM2v2.0.pdf). While suffering from numerous limitations, the POES SEM-2 MEPED measurements are long lasting, having started in 1998 and continuing to the present day. POES SEM-2 MEPED has a 90° directed telescope which sees a pitch angle range much like the DEMETER IDP instrument, and thus can be used to measure BLC fluxes when the satellite is overhead of the North Atlantic region. POES also has a 0° (BLC) telescope which is capable of measuring electron precipitation fluxes over a large range of longitudes, and latitudes (e.g., Rodger, Carson, et al., 2010). Corrections for low energy proton contamination are included in the preparation of the calibrated POES SEM-2 flux data taking into account the geometric factors of the detectors (Rodger, Clilverd, et al., 2010; Yando et al., 2011). A discussion of independent evidence that the 0° fluxes are representative of EEP and not dominated by contamination can be found in Rodger et al. (2022). For the current study we use observations from 1998 to 2020. The time resolution of the flux measurements was 2 s.

2.3. SAMPEX

SAMPEX made electron flux measurements using the Heavy Ion Large Telescope (HILT) instrument (Klecker et al., 1993; Nakamura et al., 1998). The satellite orbit was 520 × 670 km altitude, with a 82° inclination, and an orbital period of ≈96 min (Baker et al., 2012). The HILT measured radiation belt electrons fluxes >1.05 MeV. SAMPEX's HILT instrument was positioned to measure primarily DLC electron fluxes, similar to the DEMETER IDP instrument or the POES SEM-2 MEPED 90° telescope. This is discussed more in Dietrich et al. (2010), and Douma et al. (2017, 2019). For the current study we used observations from August 1996 to August 2007 (i.e., the non-spin mode period). The time resolution of the HILT flux measurements was 0.1 s.

2.4. Location of Bounce-Loss-Cone Measurements

The pitch angle populations measured by any given satellite particle detector is dependent on the orientation of the detector to the local magnetic field line. Thus, the populations vary substantially as the satellite moves along its orbit. Figure 1 is a three-panel plot of the radiation belt populations observed by the DEMETER, POES, SAMPEX particle detectors, respectively throughout their low altitude orbits. In this figure the location on the map is the projection along the satellite field line to 100 km altitude, using the IGRF 2005 model (Macmillan & Maus, 2005). The color scale represents 6 different particle populations, ranging from viewing all of the trapped and precipitating fluxes (All), to only those precipitating fluxes (FL BLC only). These categories are described in detail in Rodger, Carson, et al. (2010), and Whittaker et al. (2013). On each panel a green rectangle indicates the region in which the satellite detector views only precipitating fluxes. Typically, this region is located in the north of the Atlantic Ocean region, typically from 30°N to 60°N, and 60°W to 30°E. In the upper panel there are no flux measurements to the west at high latitude, as the DEMETER instrument was not operating in this region. In the middle panel a smaller rectangle is used for the POES 90° particle detector in order to remove the influence of Drift-Loss-Cone measurements to the western side of the box, as shown by the green dashed area. For POES and SAMPEX there are some high latitude regions where the IGRF magnetic field model returned an "open" field line result, and these areas are denoted by a very dark blue "Fail" category.

In addition to BLC measurements made in the North Atlantic we also make use of the MEPED/POES 0° directed telescope, as it is capable of measuring electron precipitation over all longitudes at the range of mid-latitudes under study here. We use this capability to make comparisons with the conclusions determined by the regionally restricted North Atlantic observations. The equivalent radiation belt populations observed by the 0° directed telescopes are shown in Figure A3 of Rodger, Carson, et al. (2010).

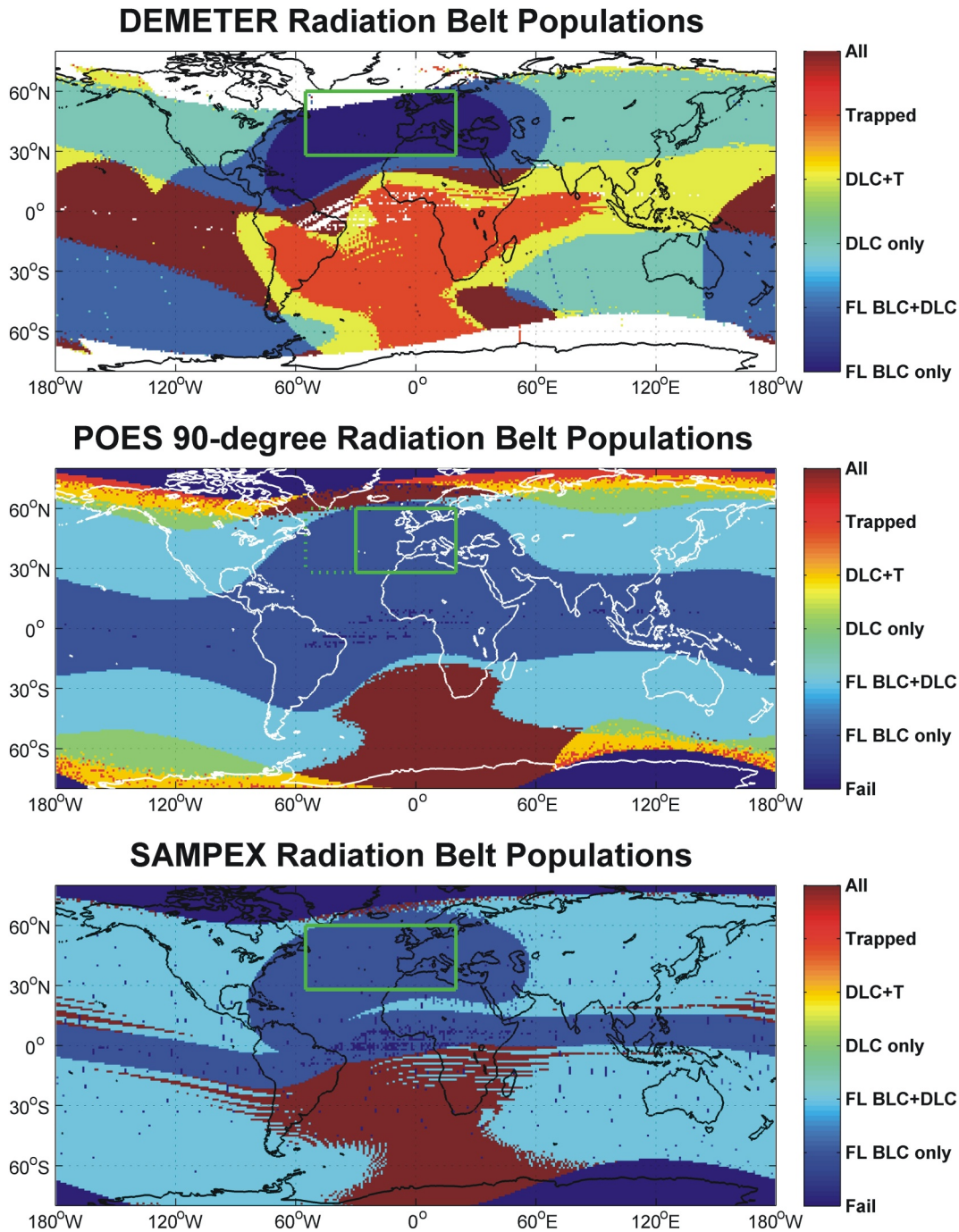

Figure 1. World map showing the changing radiation belt electron flux population observed by the three different satellites considered in this study. The upper panel is for DEMETER adapted from Whittaker et al. (2013), the middle panel is the 90° telescope carried onboard the POES SEM-2 constellation adapted from Rodger, Carson, et al. (2010), and the lower panel is for SAMPEX HILT adapted from Dietrich et al. (2010). Here T indicates trapped flux, DLC is drift-loss cone, and FL BLC is field line bounce loss cone. For most locations where there is a significant radiation belt flux, it observes a mix of DLC and FL BLC populations. The green boxes show the spatial regions selected in the current study to investigate EEP in DEMETER, 90° telescope POES, and SAMPEX HILT.

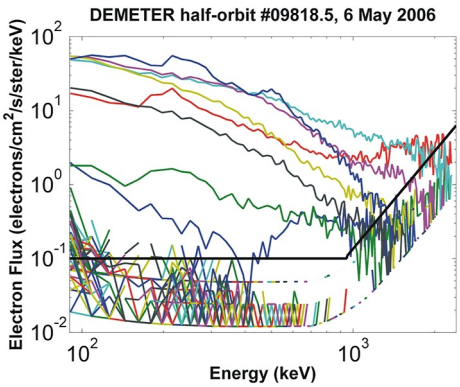

Figure 2. DEMETER IDP electron flux data from an example half orbit on 6 May 2006 displayed in 0.25-wide L-shell bins. Evidence of quantisation of low flux values near the instrument measurement floor is apparent (e.g., values occurring below the solid black line).

2.5. Scatter Factor

The main goal of our study is examine the variability in electron precipitation fluxes when binned by *L*-shell and a range of different activity indices, such that we can investigate what indices can best be used to capture the relationships, that is, a good quality (low scatter) relationship between precipitation magnitude, geomagnetic latitude, and activity driver. In order to account for the scatter in a given relationship, we determine the typical "scatter factor" for each satellite detector discussed, within the measurement region denoted by the rectangles shown in Figure 1.

The scatter factor is the geometric mean of the standard deviations of the all the flux data within a measurement bin, given by an *L*-shell versus activity index grid, for example, 0.25 L × 5 nT of Ap. We require each bin to have at least five data points. The standard deviation of all the flux values is found within each bin, and the process is repeated for all bins. Finally, the geometric (logarithmic) mean of all the standard deviations is calculated. A lower scatter factor indicates a lower overall set of standard deviations. Thus, the geomagnetic index or solar wind parameter with the lowest scatter should be a reliable way to predict which is the "best" proxy to link EEP magnitude in an L versus index/proxy relationship.

3. Calculation of the DEMETER Noise Floor

Of the three satellite particle detector instruments, the DEMETER IDP has the highest energy resolution capabilities, but historically there has been less focus on understanding the sensitivity limits of the IDP instrument than for the POES SEM-2 and SAMPEX HILT instruments. We therefore undertake an analysis of the DEMETER IDP noise floor, and how it varies with energy, as presented in this section.

Inspection of individual energy spectra in the DEMETER IDP data often show that the fluxes reported for energy bins above 800 keV are larger than those for lower energy bins. Even during very quiet geomagnetic times this relationship is observable for example, Figure 4 in Whittaker et al. (2013), and over many *L*-shell ranges. The fundamental cause of this energy dependent behavior is due to the energy-dependent variation of the IDP instrument geometric factor (Sauvaud et al., 2006). An example of the variation of IDP fluxes with energy is presented in Figure 2. Measurements from a half orbit on 6 May 2006 are shown, with colored lines representing the energy dependent fluxes for a range of 0.25 L-shell bins during this half-orbit. There are noticeable increases in IDP reported flux at higher energies (>800 keV) for some *L*-shell ranges.

Electron fluxes are computed by dividing the measured count rate in each energy bin by the energy geometry factor $G(E)$, which is described in Sauvaud et al. (2006), with units of cm^{2}sr. The IDP used a routine sampling mode with a 0.25 s^{-1} count rate. The spacing between the differential energy channels in routine mode is 17.8 keV, which gives a non-zero differential count rate minimum value of 0.014 el. s^{-1} keV^{-1} (i.e., 1 count per 4 s in a 17.8 keV bin produces a minimum value of $1/(4 \times 17.8)$). When divided by $G(E)$, this defines the instrument noise floor flux levels as exhibited in Figure 2. In addition, inspection of the fluxes close to the noise floor shows quantisation of the values. This is especially visible in the low energy/low flux regime in Figure 2 where we can see, for example, values of 1×10^{-2} or 2×10^{-2} or 3×10^{-2} el. cm^{-2}s^{-1}sr^{-1} keV^{-1} without values in between - this quantisation suggests that flux values just above the IDP instrument noise floor are still not accurate, due to the quantisation limits of the different count rate values for 1, 2, or 3 counts per time and energy range. A solid black line has been added to Figure 2 in order to indicate the flux levels below which quantisation appears to be an issue.

In order to take into account the uncertainty of the values close to the instrument noise floor, we identify an effective noise floor which ignores flux values that are inherently unreliable due to the impacts of quantisation as well as the minimum noise floor. Figure 3 reproduces the DEMETER IDP electron flux data from the half orbit on 6 May 2006 shown in Figure 2, where unreliable electron flux values have been removed. The effective noise floor is shown as a black line and can be thought of as flux values corresponding to a level of 2 counts/s in each energy bin (i.e., 8 counts in a 0.25 s sampling period), converted to flux using the instrument geometry factor. In

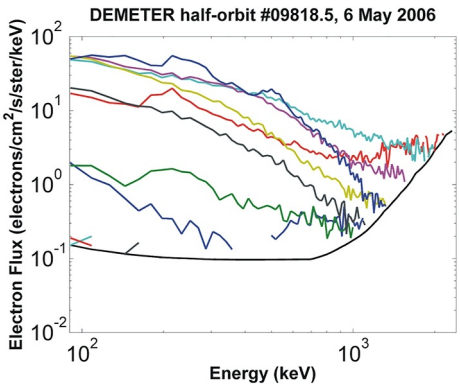

Figure 3. The calculated noise floor plotted as a solid black line on top of a series of energy spectra taken from an example DEMETER half orbit on 6 May 2006. The effective noise floor, based on a threshold of 2 counts/s in the IDP detector has been used to discard unreliable flux values.

our analysis electron flux values that are unlikely to be meaningful measures of flux are discarded using this effective noise floor.

For the POES SEM-2 detector the effective noise floor has previously shown to be at 1 count/s (Rodger, Clilverd, et al., 2010; Yando et al., 2011). In this study the noise floor is not a significant issue for SAMPEX HILT due to the very large geometric factor detector, which was designed to provide accurate flux measurements even at 20 ms sampling (Klecker et al., 1993).

4. Results

In this section two energy ranges are considered: medium energy (Section 4.1) and high energy (Section 4.2). Here, medium energy precipitation is investigated using integral >90 keV or >100 keV electron precipitation fluxes —depending on the detector. For the DEMETER data all of the IDP 124 differential energy channels were combined to give an integral flux value >90 keV, while for POES the >100 keV integral channel was used as a comparison. Both detectors measure energies up to about >2 MeV. For the high energy analysis only the DEMETER energy channels >700 keV were combined to give an integral value. The POES *E*4 >700 keV channel was used as a comparison, as well as the >1.05 MeV SAMPEX HILT data.

Four geomagnetic activity indices are considered in terms of their link to electron precipitation at this energy, that is, Ap, Kp, Dst, and AE. Ap and Kp have a fundamental time resolution of 3 hr, while Dst and AE have hourly resolution. Three solar wind indices are also considered, that is, solar wind velocity (*Vx*), southward interplanetary magnetic field (*Bz*), and the solar wind dynamic pressure (*Pdyn*). The solar wind data have 1 min time resolution and are expressed in GSM coordinates.

The electron precipitation flux measurements sampled within each 0.25 L-shell section of the orbital path through the region sampled. Typically, the time taken for the satellites to fly through a 0.25 L wide section at $L \sim 4$ or so is in the order of 1 min, so many flux measurements were combined for each section, depending on the instrument sampling rate. Each average flux value was then associated with the geomagnetic and solar wind index parameters at the average time of the measurements. Since the indices are recorded with 3-hourly, hourly or minute resolution we used linear interpolation to infer an index value to coincide with the time that the average flux was recorded. This interpolation was done with all of the geomagnetic indices and solar wind parameters. Once flux/index pairs were calculated for each 0.25 L-shell section in each orbit through the region of interest they can be binned by activity level. An analysis of the scatter factors per activity bin can then be made. The subsections below describe such analysis for the medium and high energy fluxes.

4.1. Electron Precipitation >90 keV

The bounce-loss-cone binned electron precipitation fluxes from the DEMETER IDP instrument are shown in Figure 4, determined from within the North Atlantic sample region shown in Figure 1. The four panels show the results for AE, Kp, Dst, and Ap geomagnetic indices respectively, with the color scale representing the logarithm of the mean flux in each bin. White colors indicate bins with no data, while colored areas with white dots indicate bins where the flux magnitude was comparable to the standard deviation, that is, high variability within the bin. These conditions typically occur where precipitation fluxes are very low. Black lines represent the L-shell of the plasmapause as a function of each geomagnetic index using the formulations given by O'Brien and Moldwin (2003). We note that O'Brien and Moldwin do not provide a plasmapause model for Ap, hence the lack of a black line in this panel.

In each panel of Figure 4 the occurrence of the largest fluxes is concentrated toward the highest geomagnetic activity levels, and toward the highest range of the *L*-shell bins. There is some overlap with high precipitating fluxes and the location of the plasmapause, although DEMETER rarely sampled at L-shells high enough to investigate locations outside the plasmapause. There is an indication of precipitating fluxes moving to lower L for increasing geomagnetic activity, consistent with the plasmapause moving inwards toward low *L*-shells (Carpenter & Anderson, 1992). The Dst panel in particular shows a tendency for the flux pattern to follow the behavior of the plasmapause, with flux levels dropping by approximately two orders of magnitude within 1.5 L (6 bins) inside of

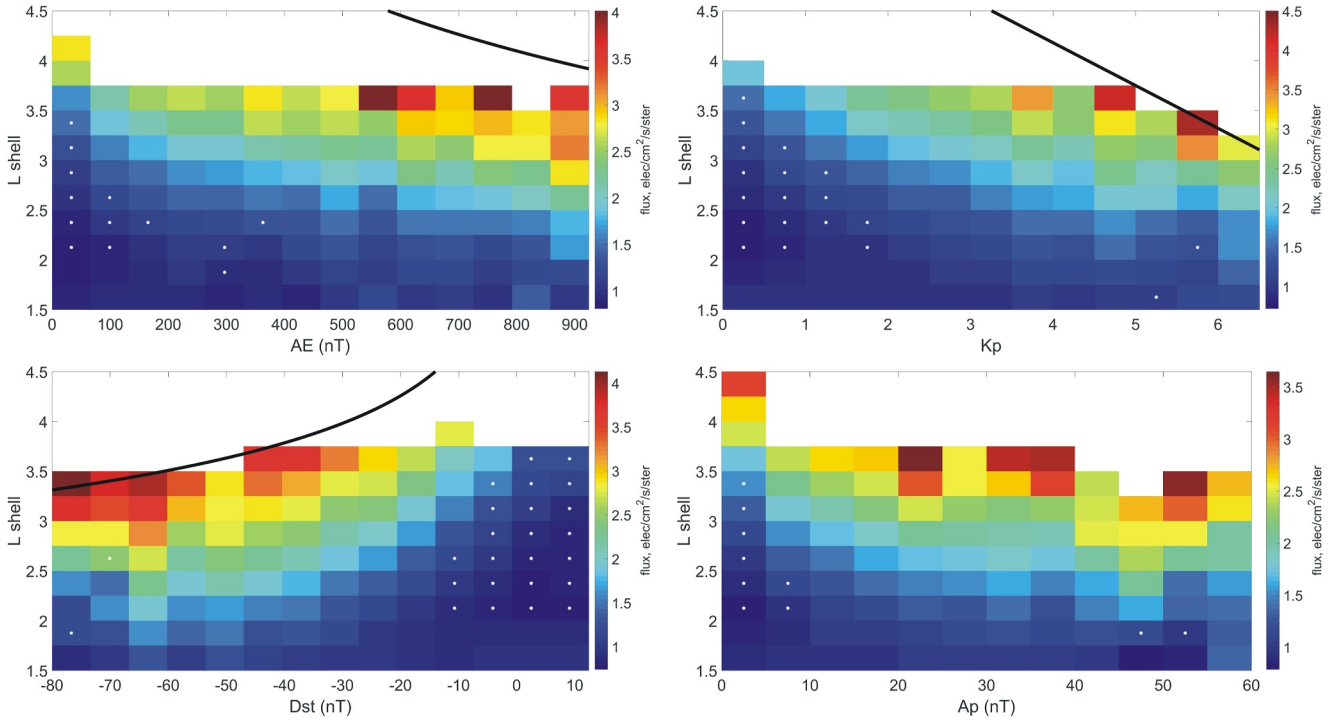

Figure 4. The variation of DEMETER >90 keV electron precipitation fluxes with L-shell and geomagnetic activity. Four panels represent the AE, Kp, Dst, and Ap index variations. The black lines indicate the location of the plasmapause for three of the different geomagnetic indices, using the formulations given in O'Brien and Moldwin (2003).

the plasmapause at all geomagnetic activity levels. Very low values of the >90 keV flux were seen below $L = 2.5$ for the majority of geomagnetic conditions.

POES >100 keV precipitation fluxes in the North Atlantic sample region are shown in Figure 5. The panels are the same format as shown in Figure 4, except that they extend to more disturbed geomagnetic conditions. As the POES SEM-2 dataset is very long-lasting, it spans a wider range of disturbed conditions. Additionally, each bin has fluxes that are high enough that they are larger than the standard deviation in the bin and thus no white dots appear. This also true for Figures 6 and 9 shown later in the manuscript. The fluxes shown in Figure 5 are based on the POES 90° detector viewing the BLC in the sample region shown in Figure 1. The panels contain flux values up to slightly higher *L*-shells than was visible in the equivalent DEMETER panels, and thus give a somewhat more complete picture of the variations of flux at *L*-shells higher than the plasmapause. Both satellite datasets show flux values of $\sim 10^4$ el.cm^{-2}s^{-1}sr^{-1} in the vicinity of the plasmapause. However, the POES >100 keV precipitating fluxes are clearly larger outside the plasmapause when contrasted with near the plasmpause. As with the DEMETER panels, larger electron precipitation fluxes occur during higher geomagnetic activity levels, but more detailed analysis is needed to discern which index provides a better correlation with the fluxes. This will be investigated in detail at the end of this subsection.

DEMETER IDP and the POES SEM-2 90° telescope only views the BLC in the North Atlantic region, allowing direct comparisons of these measurements in that sampling region. However, it is possible to use the SEM-2 0° telescope on POES to study the BLC precipitation electron fluxes over all longitudes to provide another comparison. Figure 6 shows the >100 keV integral electron precipitation fluxes from the SEM-2 0° telescope using all longitudes, and also investigating higher *L*-shells as that is possible for this dataset. The figure is otherwise in the same format as Figures 4 and 5. The main differences between the global 0° POES data plot (Figure 6) compared with the North Atlantic 90°POES data plot (Figure 5) is that the panels include a wider range of geomagnetic activity and L-shell—his is caused by the larger dataset available when using measurements made spanning all longitudes (i.e., the 0° POES data). Additionally, the slightly restrictive North Atlantic upper latitude limit for POES 90°precipitating flux (shown in Figure 1) reduces the 90-deg observations for $L > 5$. However, where the two plots overlap in geomagnetic activity and L-shell both figures agree regarding flux distributions peaking in

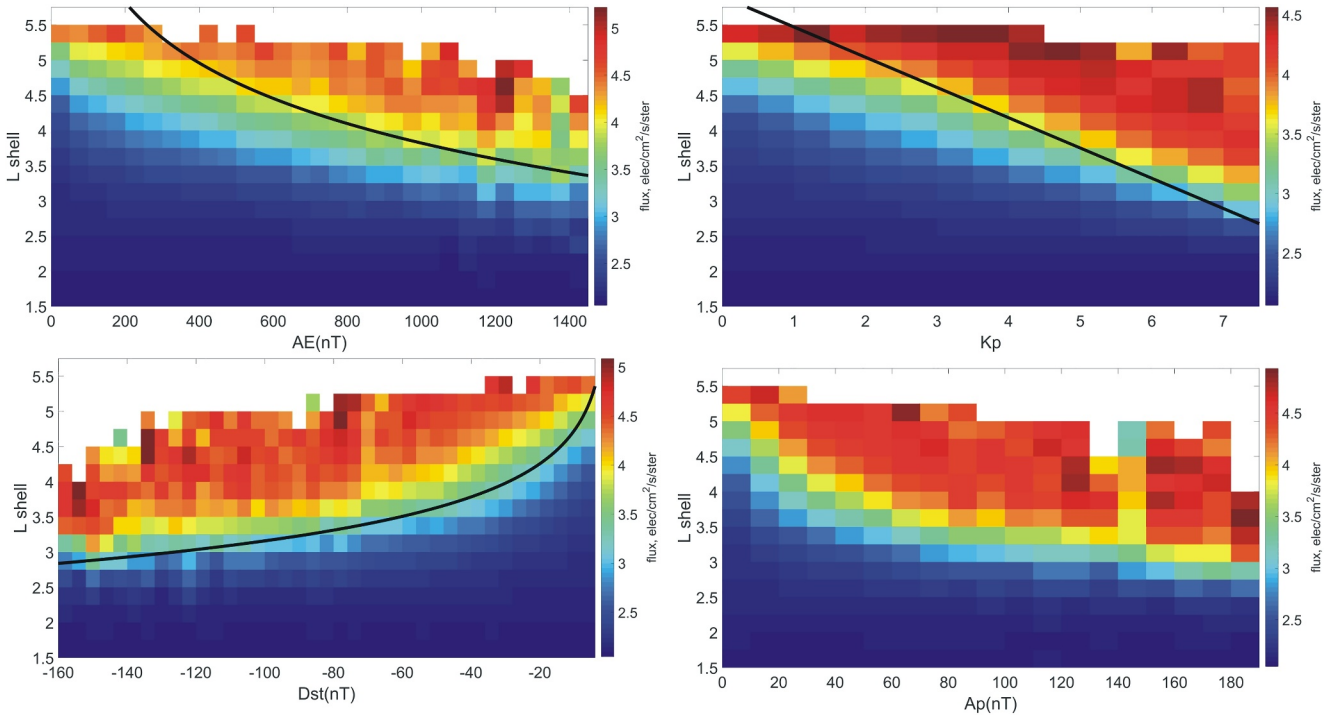

Figure 5. The variation of POES >100 keV electron precipitation fluxes with L-shell and geomagnetic activity, for the 90° detector viewing the North Atlantic sample region, in the same format as Figure 4.

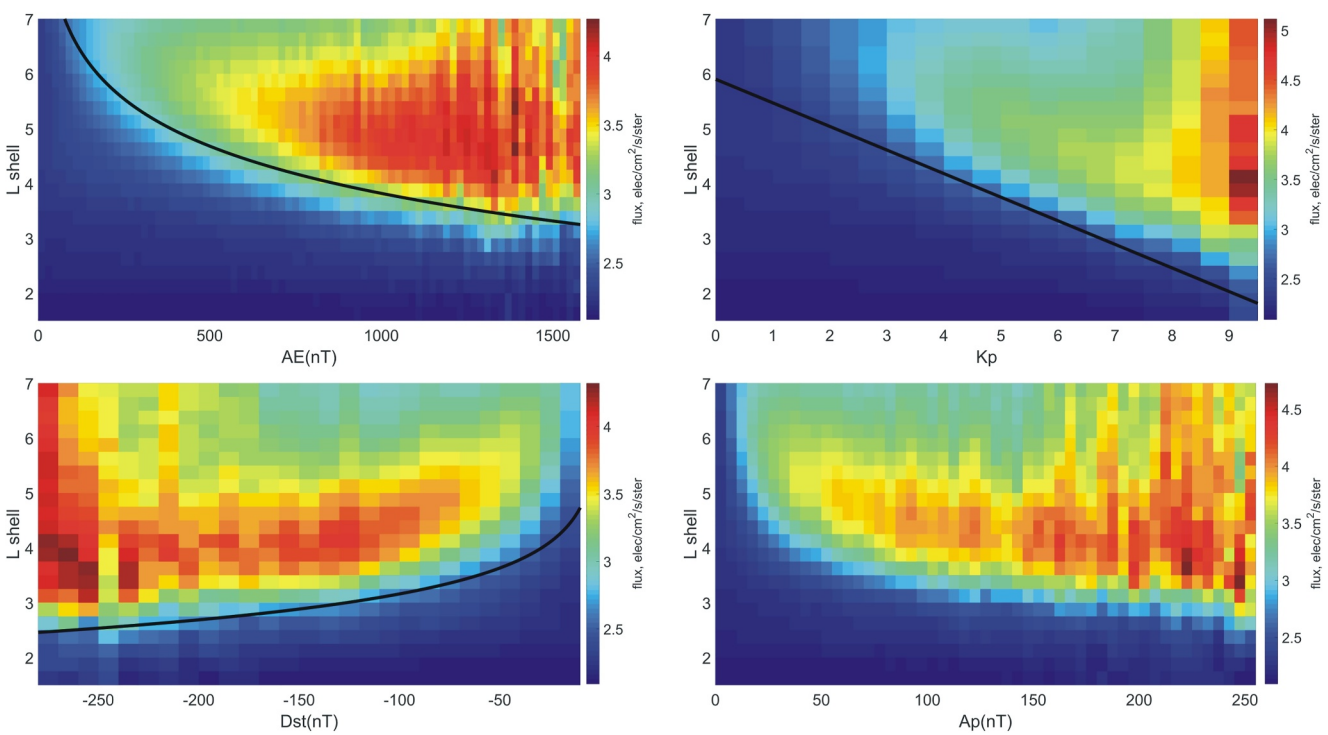

Figure 6. The variation of POES >100 keV 0°detector electron precipitation fluxes with L-shell and geomagnetic activity. In this case all longitudes are included. Otherwise the plot is in the same format as Figure 4.

Table 1
The Scatter Factors for Medium Energy Electron Precipitation Derived From the Standard Deviations of Three Precipitating Electron Flux Datasets When Binned by L-Shell and Activity Index

	DEMETER >90 keV	POES >100 keV	POES >100 keV
	IDP	90° detector	0° detector
	North Atlantic	North Atlantic	Worldwide
	$1.5 < L < 4.5$	$1.5 < L < 5.5$	$1.5 < L < 7$
	Scatter factor × 10^{-2} (cm^{-2} s^{-1} sr^{-1})	Scatter factor × 10^{-3} (cm^{-2} s^{-1} sr^{-1})	Scatter factor × 10^{-3} (cm^{-2} s^{-1} sr^{-1})
INDEX			
Geomagnetic			
Ap (3 hr)	11.4 ± 0.7	*2.5 ± 0.1*	**3.4 ± 0.1**
Dst (1 hr)	**9.7 ± 0.5**	**2.3 ± 0.1**	*4.3 ± 0.2*
Kp (3 hr)	11.6 ± 0.6	3.6 ± 0.2	4.8 ± 0.2
AE (1 hr)	11.9 ± 0.6	3.8 ± 0.2	5.9 ± 0.1
Solar Wind/IMF			
V_x (1 min)	20.9 ± 1.1	3.9 ± 0.2	5.5 ± 0.2
B_z (1 min)	26.2 ± 1.4	6.1 ± 0.3	10.3 ± 0.6
P_{dyn} (1 min)	21.3 ± 1.1	6.2 ± 0.3	8.9 ± 0.4

Note. Indices are separated into Geomagnetic and Solar Wind parameters. The activity parameter with the smallest (i.e., best) scatter factor is highlighted in bold and underlined, while the next best result is indicated through italics with underlining. The standard error of each scatter factor is shown as a ±value. See text for more details.

the vicinity of the plasmapause. As in the previous figures, the electron precipitation fluxes are larger at *L*-shells outside of the plasmapause, and larger for more disturbed geomagnetic conditions. However, precipitating flux values are seen to decrease at the highest L-shells. This is because as the influence of radiation-belt precipitation loss processes tends to become less dominant (e.g., Section 3 of Ripoll et al., 2020). It is likely that at the very highest geomagnetic activity levels the fluxes are dominated by substorm-induced electron precipitation, resulting in a wider *L*-shell spread and higher fluxes, than seen for less active conditions. This suggestion is supported by the earlier work of Cresswell-Moorcock et al. (2013) and Rodger et al. (2022), who both used superposed epoch analysis of POES measurements to show evidence of electron precipitation from substorms extending beyond $L > 10$.

In order to compare the three measurement scenarios illustrated above, scatter factor analysis as described in Section 2.5 was undertaken. The results of this analysis is presented in Table 1. Geometric mean standard deviations (STD) are shown along with their standard error (SE) where SE = STD/$\sqrt{}$(number of samples). Summary details for each of the three satellite-measurement scenarios are given at the top of the columns. The indices under investigation are grouped into two categories: Geomagnetic, and Solar Wind/IMF (Interplanetary Magnetic Field),. The solar wind/IMF parameters are the *x*-component of solar wind velocity (*Vx*), the magnetic field z-component (*Bz*), and the solar wind dynamic pressure (*Pdyn*), all expressed in GSM coordinates.

In Table 1 the parameter with the smallest scatter factor for each satellite dataset is highlighted in bold and underlined. The next best scatter factor is indicated through italics with underlining. This highlighting has been undertaken separately for the fundamental time resolution of each index. The Ap and Dst indices consistently generate the lowest scatter factors in all three datasets. As is visually apparent from Figures 4–6 the DEMETER dataset has higher scatter values for each individual index when compared with the equivalent POES datasets. In Table 1, none of the solar wind/IMF parameters result in scatter factors that occur in the two smallest scatter factors, that is, the two best indices.

The standard errors shown in Table 1 provide an indication of the uncertainty in the scatter factor values. As an example, for the POES >100 keV 90° detector (middle) column the Dst and Ap indices have scatter factors of 2.3 ± 0.1 and 2.5 ± 0.1. The error associated with these scatter factor values is substantially smaller than the difference between the two top indices and the next best values (3.6 ± 0.2 for Kp). This is true for Ap and Dst in the POES worldwide dataset (right hand column) and for Dst in the DEMETER (left hand) column. For

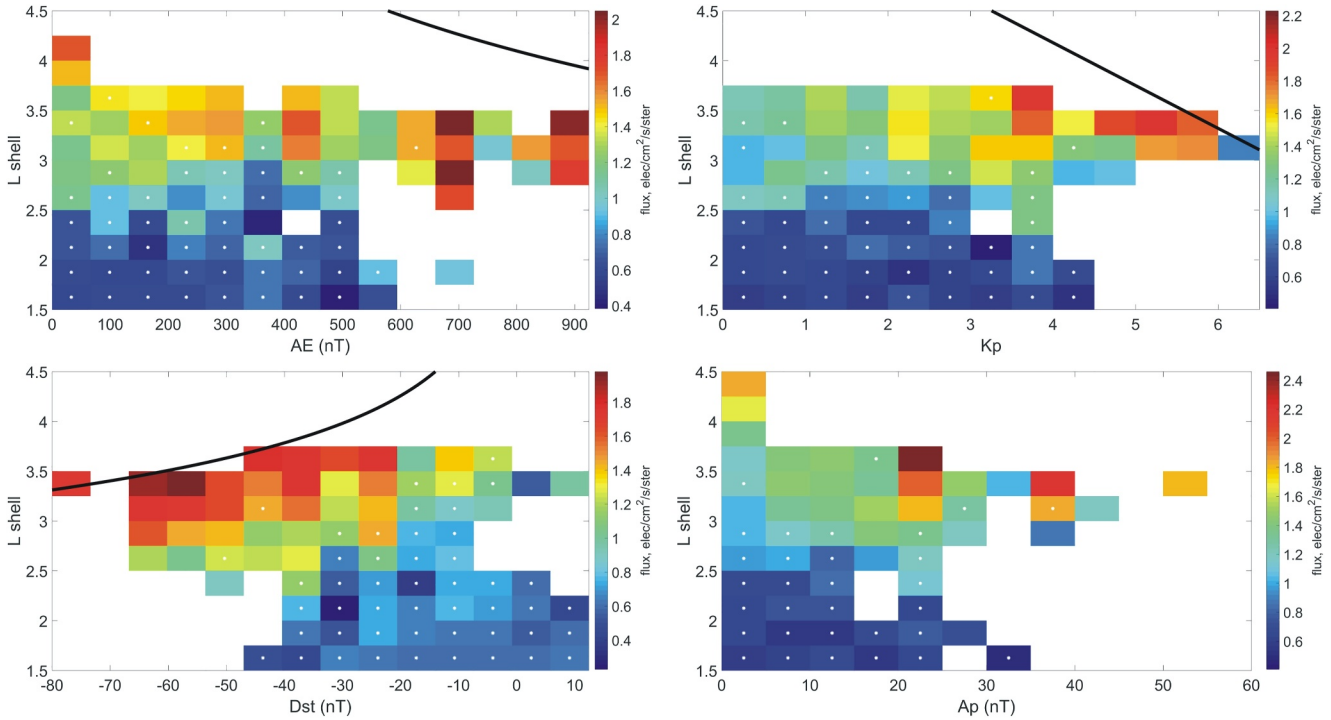

Figure 7. As for Figure 4, but plotting >700 keV DEMETER electron precipitation fluxes in the North Atlantic sampling region.

DEMETER the standard errors in the scatter factors for Ap, Kp, and AE are such that there is no clear distinction between them, and so no index has been highlighted as the next best scatter factor, that is, no parameter is underlined and in italics.

The indices analyzed in Table 1 have a wide range of time resolutions, from 1 min to 3 hr. However, the index values are determined at the time of each flux measurement. In order to test for potential delay times between the most active periods and electron precipitation flux variations the analysis was repeated, testing for the maximum disturbance value (either a maximum or minimum value depending on the parameter) in the 24 hr prior to the flux measurement. This is consistent with the normal definition of Ap* (Allen & Wilkinson, 1993) which has been used as a measure of a geomagnetic storm peak intensity. The scatter factors for medium electron precipitation energies using maximum 24-hr disturbance indices are presented in Table S1 in Supporting Information S1. Colored fonts are used to indicate whether the scatter factor for any particular index has increased or decreased compared with the values shown in Table 1, for example, the scatter factor for the DEMETER fluxes increases from 11.4 (Ap) to 13.8 (Ap*) when the index is analyzed over 24 hr, as denoted by a red font. Blue fonts indicate a reduction in scatter factor over 24-hr timescales suggesting a smaller standard deviation between the fluxes and the 24-hr index. Generally, the best and second-best parameters remain Ap* and Dst* as good proxies for medium energy electron precipitation despite the different method used in index value selection.

4.2. Electron Precipitation >700 keV

In this section the analysis techniques of the previous section is repeated, but for higher energy electron precipitation fluxes (i.e., >700 keV) rather than for medium energies. As DEMETER IDP has 126 differential energy channels it is possible to combine the highest energy channels and produce an integral flux >700 keV. Figure 7 shows results of plotting *L*-shell versus geomagnetic indices AE, Kp, Dst, and Ap in the same format as Figure 4 but for the high energy electron precipitation measured by DEMETER in the North Atlantic sample region. In this energy range the data tend to be sparse as few DEMETER measurements have integrated flux values higher than the effective noise floor. However, as before, high fluxes are observed when the index of activity increases. Note that the flux color-scale maxima are significantly lower than the equivalent panels in Figure 4.

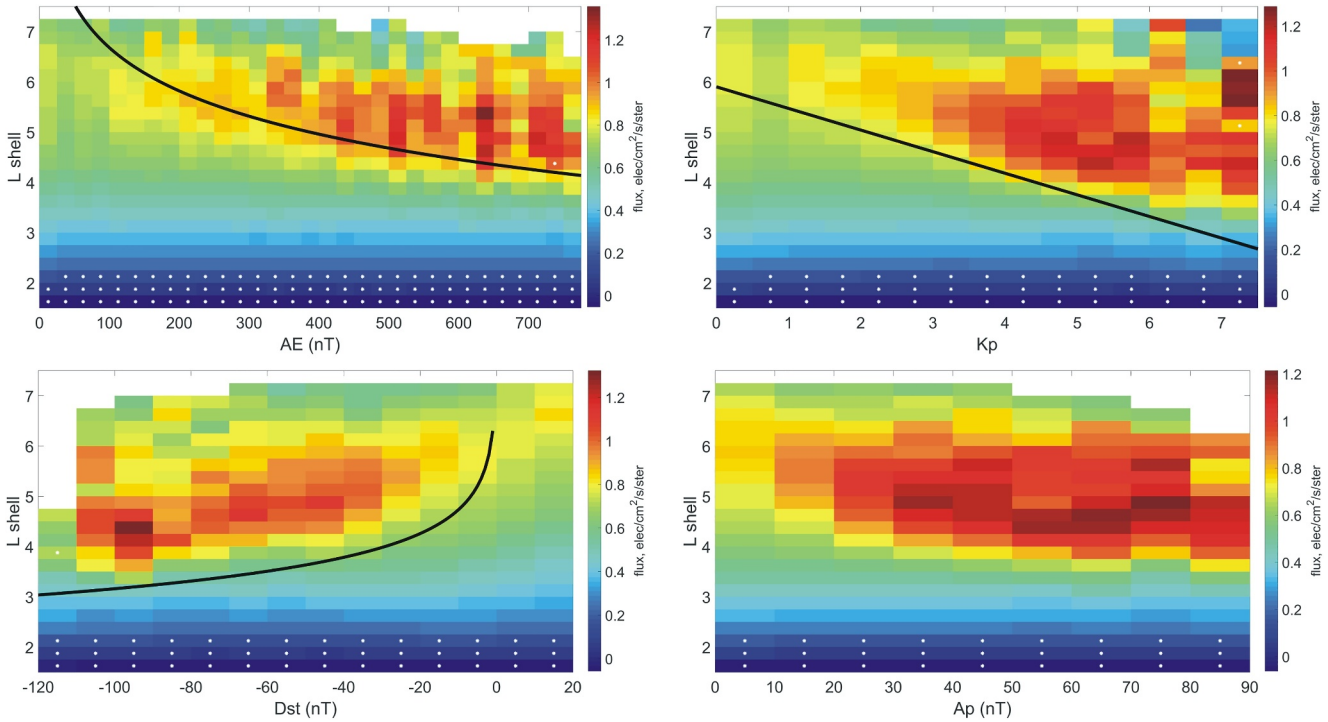

Figure 8. The variation of SAMPEX HILT >1.05 MeV electron precipitation fluxes with L-shell and geomagnetic activity, for the North Atlantic sample region. Same format as Figures 4–7.

Further analysis of high energy electron precipitation is provided by SAMPEX HILT measurements in the North Atlantic sampling region, where the detector is measuring fluxes within the BLC. Figure 8 shows the SAMPEX data plotted in the same format as Figure 7. High energy fluxes tend to be larger at more disturbed levels of geomagnetic disturbance and associated with regions just outside of the plasmapause; clearly, this is consistent with previous figures. Figure 8 covers the L-activity space much more comprehensively than Figure 7. A very significant factor in this is lack of DEMETER coverage above 65° latitude, which limits L-shell range of Figure 7 (DEMETER) relative to Figure 8 (SAMPEX). DEMETER collected data for ∼6.5 years in comparison to SAMPEX's 11 years of non-spin period observations. In addition, the DEMETER operational period was also much geomagnetically quieter than SAMPEX sampled, with significant time periods where the radiation belts had largely faded away (Rodger et al., 2016).

As a final comparison, the POES SEM-2 *E*4 >700 keV 0° detector is used to provide a measure of high energy electron precipitation flux over all longitudes. Figure 9 shows the POES >700 keV electron precipitation fluxes in the same format as the SAMPEX data shown in Figure 8. Note that although the L-shell range is the same as in Figure 8, the geomagnetic index ranges are quite different. This is a result of examining the 22+ years of POES data, leading to a larger range of geomagnetic disturbance level, compared with the 11 years of SAMPEX data analyzed. The distributions in Figure 9 (POES *E*4 >700 keV 0°, all longitudes) look different from the distributions in Figure 8 (SAMPEX >1.04 MeV, North Atlantic) because of the wider range of geomagnetic activity incorporated in the more extensive POES 0°dataset. For example, the Dst panel in Figure 8 shows a lowest value of −120 nT while in Figure 9 Dst goes down to −275 nT. Where the two panels overlap in geomagnetic activity and L-shell there are similar flux distributions. This is also seen in the other comparable panels for Figures 8 and 9. Although there is some visual correspondence of enhanced flux in the vicinity of the plasmapause location, the panels of Figure 9 are dominated by high flux, wide L-shell range features, at the highest magnetic disturbance levels. A comparison between POES 0° > 100 keV (Figure 6) and >700 keV precipitation fluxes (Figure 9) shows more banded structure at the higher energies than the lower ones. These features are possibly due to substorm-induced precipitation, or possibly electro-magnetic ion-cyclotron (EMIC) wave-induced precipitation (e.g., Cresswell-Moorcock et al., 2013; Usanova et al., 2014). In Figure 9 the Kp panel's high activity, high flux

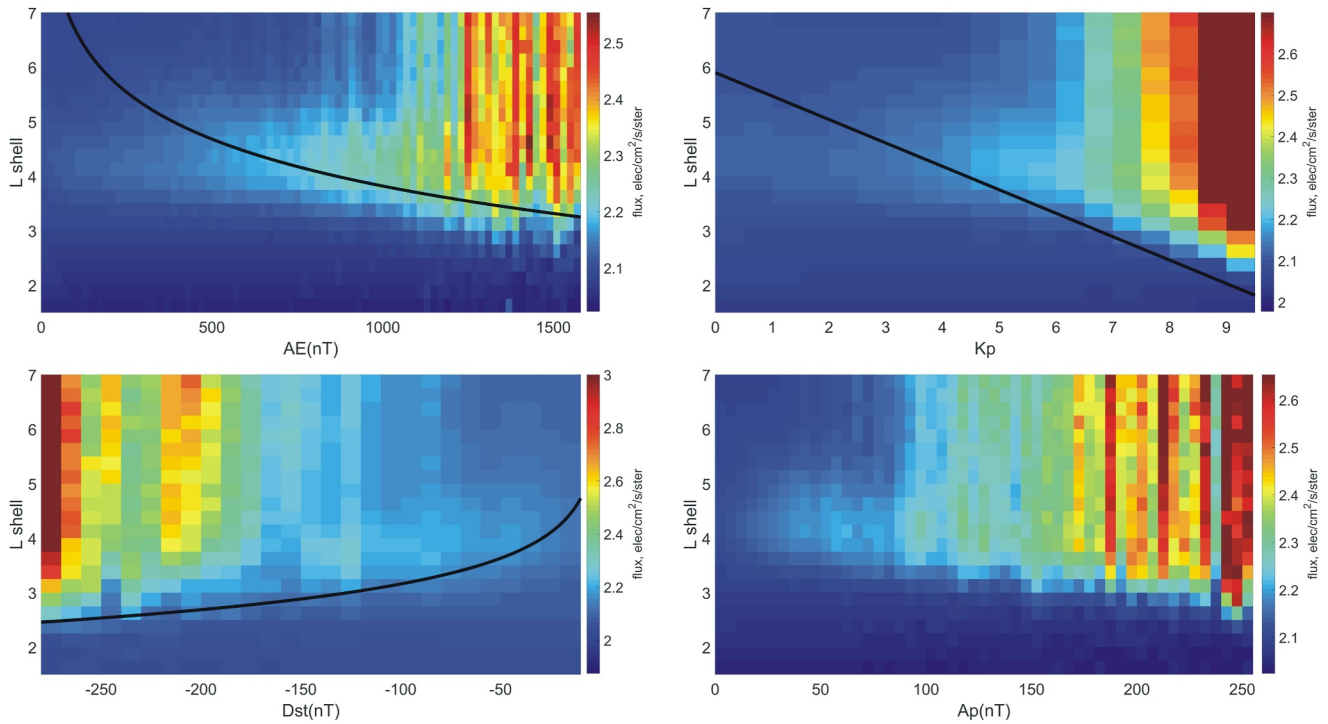

Figure 9. The variation of POES SEM-2 E4 0˚detector >700 keV electron precipitation fluxes with L-shell and geomagnetic activity. This includes observations from all longitudes, in the same format as Figure 8.

distributions are much smoother, and do not show such banded structure, which is most likely due to the Kp index parameter resolution.

Scatter factor analysis of high energy electron precipitation (>700 keV) for the three measurement scenarios is given in Table 2. This table is the same format as Table 1, although now including datasets from DEMETER, POES and SAMPEX. The two indices giving the lowest scatter values, that is, best, are highlighted as before. Here Kp is identified as the index with the least scatter over a range of scenarios, with AE the next best. Notably there is a range of contenders coming from the DEMETER measurements, with Ap the best at original time resolutions. Also notably, one of the solar wind/IMF parameters features in the "best" highlighting, with *Vx* a close second for POES >700 keV measurements. Taking into account the standard error values for each scatter factor suggests that some of the solar wind parameters are potentially as good a proxy for >700 keV electron precipitation flux as the geomagnetic indices. Table S2 in Supporting Information S1 shows the scatter factors for the maximum disturbance value (either a maximum or minimum value depending on the parameter) in the 24 hr prior to the flux measurement. This tests for potential delay times between the most active periods and electron precipitation flux variations. Generally, the best and second best parameters remain Kp and AE as good proxies for high energy electron precipitation despite the different method used in index value selection.

5. Discussion

Scatter factor analysis, based on the standard deviation between electron precipitation flux and geomagnetic indices/solar wind parameters, has been used to determine the most reliable proxies to empirically capture the variation of electron precipitation. The calculation of scatter factor was undertaken for a wide range of geomagnetic latitude (given by *L*-shell) and activity level. Tables 1 and 2 summarize the results of the scatter factor analysis for medium energy electron precipitation (100's of keV) and for high energies (~1 MeV), using several different satellites/instruments. The scatter factors of the DEMETER IDP >90 keV integrated measurements are approximately a factor of 30 larger than the POES >100 keV integral measurements. This is most likely due to instrumental differences, in combination with a bias toward lower L-shell for DEMETER measurements. The scatter factors for the SAMPEX HILT measurements are also larger than the POES ones, most likely due to the large geometric factor of the HILT instrument. These factors make the inter-comparison of

Table 2
The Scatter Factors for High Energy (>700 keV) Electron Precipitation Derived From the Standard Deviations of Three Electron Flux Measurement Scenarios When Binned by L-Shell and Index of Activity

	DEMETER >700 keV	POES >700 keV	SAMPEX >1.05 MeV
	IDP	P6 0° detector	HILT
	North Atlantic	Worldwide	North Atlantic
	$1.5 < L < 4.5$	$1.5 < L < 7$	$1.5 < L < 7.25$
	Scatter factor $\times 10^{-2}$ ($cm^{-2}s^{-1}sr^{-1}$)	Scatter factor $\times 10^{-3}$ ($cm^{-2}s^{-1}sr^{-1}$)	Scatter factor $\times 10^{-2}$ ($cm^{-2}s^{-1}sr^{-1}$)
INDEX			
Geomagnetic			
Ap (3 hr)	**32.6 ± 1.9**	11.5 ± 0.3	56.0 ± 3.5
Dst (1 hr)	37.0 ± 2.0	11.0 ± 0.4	56.3 ± 2.9
Kp (3 hr)	34.8 ± 1.9	**9.8 ± 0.5**	**53.3 ± 2.7**
AE (1 hr)	*33.8 ± 1.8*	11.5 ± 0.3	*54.8 ± 1.9*
Solar Wind/IMF			
V_x (1 min)	40.6 ± 2.1	*10.3 ± 0.5*	55.4 ± 3.0
B_z (1 min)	44.1 ± 2.3	11.7 ± 0.6	60.9 ± 3.3
P_{dyn} (1 min)	40.2 ± 2.1	11.5 ± 0.5	59.1 ± 3.4

Note. The activity parameter with the smallest (best) scatter factor is highlighted in bold and underlined, while the next best result is indicated through *italics with underlining*. The standard error of each scatter factor is shown as a ±value. Format is the same as Table 1. See text for more details.

scatter factors between instruments (i.e., different columns in the tables) very difficult. However, the electron precipitation flux dataset are the same for each column in the tables. As such, they can be compared to find the best proxy for each dataset, and inter-dataset comparisons undertaken.

In order to test for potential delay times between the most active periods and electron precipitation flux variations the analysis was repeated, testing for the maximum disturbance value (either a maximum or minimum value depending on the parameter) in the 24 hr prior to the flux measurement. These results are provided in Tables S1 and S2 in Supporting Information S1. Overall, there was a small reduction in scatter factor using the 24-hr indices (peak disturbance value), with the most notable change occurring for the solar wind parameters, that is, −13% for the medium energy results. This can be seen through the preponderance of blue coloring of the solar wind values in the lower sections of Tables S1 and S2 in Supporting Information S1. No clear change occurred for scatter factors calculated with the 24-hr geomagnetic indices (shown by a mixture of red and blue fonts). Converting from hourly index values to 24-hr maximum (minimum) values makes almost no difference to the scatter factors, which suggests that electron precipitation flux process timescales last hours rather than minutes. Despite the improvement of the scatter factors for the 24-hr solar wind results, the same 'best' proxies for medium and high energy electron precipitation were identified by both the fundamental time resolution and 24-hr maximum disturbance analysis.

Despite using three different low-Earth orbiting satellites, and a range of differing detector viewing configurations, the scatter factor analysis undertaken in this study shows consistent identification of the best proxies to empirically represent electron precipitation. For the medium energy electron precipitation (several tens to hundred's of keV) the best proxies are Ap and Dst. For the high energy electron precipitation (~1 MeV) the best proxies are Kp and AE. These findings are independent of the time resolution of the proxy. While there are different ranges of geomagnetic activity exhibited by each satellite dataset they consistently identify Dst and Ap as the top two proxy indices for describing the medium energy precipitation flux variability, along with Kp and AE for the high energy proxy. This suggests a consistency in the application of a given energy proxy over a wide range of geomagnetic activity.

The identification of Ap and Dst as the best proxies for the medium energy electron precipitation is consistent with the injection and transport of mid (i.e., seed) and low-energy (i.e., source) electrons into the inner magnetosphere which occurs during enhanced solar wind and geomagnetic activity. Precipitation of mid energy

electrons is primarily through processes dominated by VLF waves, particularly chorus occurring just outside of the plasmapause (van de Kamp et al., 2016; Whittaker et al., 2014). Ap is a good measure of convection (Thomsen, 2004) and Dst indicates increased transport (e.g., Zhao & Li, 2013) consistent with this chorus-driven precipitation framework.

The identification of Kp and AE as the best proxies for high energy electron precipitation can also be considered within the framework of chorus whistler mode wave drivers of seed electrons (hundreds of keV electrons) accelerating them to produce relativistic electrons (Jaynes et al., 2015). Kp is a measure of convection, and AE indicates substorm activity. Convection associated with substorms will generate intense chorus producing relativistic electron microburst precipitation (Douma et al., 2017, 2019) and also EMIC waves which also produce relativistic electron precipitation (Blum et al., 2015; Jaynes et al., 2015; Hendry et al., 2017 and references therein).

6. Conclusions

Empirical models of energetic electron precipitation forcing (EEP) have been made using geomagnetic indices as proxies. The EEP forcing models need to be suitable for incorporation into coupled-climate model runs and allow for periods outside the current satellite era to be included in the climate model runs. In the current study the suitability of a range of proxies to represent EEP fluxes is investigated, using three different satellite electron precipitation datasets (DEMETER, POES, and SAMPEX). In order to measure electron precipitation fluxes without the dominating effects of much larger trapped fluxes being incorporated, we primarily focused on measurements made above the North Atlantic region. This was always the case for DEMETER and SAMPEX observations, whereas the POES bounce-loss-cone measurements had the capability of more global analysis.

In order to take into account the noise floor of the DEMETER IDP measurements an estimate of the sensitivity of each highly resolved energy channel was made. The description of the DEMETER IDP effective noise floor provided a route through which only realistic fluxes were included in the suitability analysis.

The suitability of each proxy to represent EEP fluxes was found using a scatter factor which summarized the EEP flux variations over a wide *L*-shell range (i.e., geomagnetic latitude) and a wide range of activity levels. The scatter factor for each satellite/proxy combination was calculated through the geometric mean of the standard deviations of the all the flux data within each measurement bin given by an *L*-shell versus activity index grid. Lower scatter factors are indicative of a lower overall set of standard deviations, and were used to identify the most appropriate proxy. A standard error of each scatter factor was calculated and used as an indication of the uncertainty in the scatter factor results. This analysis was undertaken for four geomagnetic indices (Ap, Dst, Kp, AE), and for 3 solar wind/IMF parameters (*Vx*, *Bz*, *Pdyn*).

The scatter factor analysis shows consistent identification of the best proxies for electron precipitation, even using three different low-Earth orbiting satellite datasets, and a range of detector viewing configurations. For the medium energy electron precipitation (several tens to hundred's of keV) the best proxies are Ap and Dst. For the high energy electron precipitation (∼1 MeV) the best proxies are Kp and AE.

The identification of the Ap index as the best proxy for medium energy EEP is a vindication of the approach taken by Van De Kamp et al. (2016) to provide an EEP forcing capability in Matthes et al. (2017). The van de Kamp flux model described EEP fluxes over a range of 10 keV to 1 MeV. The results found here suggest that while Ap is a good proxy for most of that energy range, it is likely that for electron energies >700 keV an index more associated with substorm activity (such as AE) would be more appropriate.

Data Availability Statement

The data used in this paper are available at the CNES/CESR Centre de Donnees pour la Physique des Plasmas (CDPP - Demeter IDP, https://cdpp-archive.cnes.fr/user/cdpp/modules/1723) and NOAA's National Geophysical Data Center (NGDC - POES MEPED data, https://ngdc.noaa.gov/stp/satellite/poes/). Data availability for SAMPEX is described at.

http://www.srl.caltech.edu/sampex/DataCenter/index.html. The Solar Wind parameters were obtained from https://solarscience.msfc.nasa.gov/SolarWind.shtml. Accessed: 2021-05-25.

AE, Ap, Dst, and Kp geomagnetic activity indices were downloaded from the UK Solar System Data Centre (https://www.ukssdc.ac.uk/). Dynamic pressure (Pdyn), solar wind velocity (Vx), and interplanetary magnetic field (Bz) data were obtained from the SuperMAG website (https://supermag.jhuapl.edu/); for the use of these parameters we gratefully acknowledge the SuperMAG collaborators (https://supermag.jhuapl.edu/info/?page=acknowledgement)

Acknowledgments
The authors wish to thank the personnel who developed, maintain, and operate the NOAA/POES spacecraft and also those who supported the earlier DEMETER and SAMPEX satellites.

References

Agapitov, O. V., Artemyev, A. V., Mourenas, D., Mozer, F. S., & Krasnoselskikh, V. (2015). Empirical model of lower band chorus wave distribution in the outer radiation belt. *Journal of Geophysical Research: Space Physics*, *120*(12), 10425–10442. https://doi.org/10.1002/2015ja021829

Allen, J. H., & Wilkinson, D. C. (1993). *Solar-terrestrial activity affecting systems in space and on Earth. In Solar-terrestrial predictions-IV: Proceedings of a Workshop at Ottawa, Canada May 18-22, 1992. In Hruska, J., Shea, M. A., Smart, D. F., & Heckman, G. (Eds.).* (pp. 75–107). National Oceanic and Atmospheric Administration.

Andersson, M. E., Verronen, P. T., Marsh, D. R., Seppälä, A., Päivärinta, S.-M., Rodger, C. J., et al. (2018). Polar ozone response to energetic particle precipitation over decadal timescales: The role of medium-energy electrons. *Journal of Geophysical Research: Atmospheres*, *123*(1), 607–622. https://doi.org/10.1002/2017JD027605

Baker, D. N., Mazur, J. E., & Mason, G. (2012). SAMPEX to reenter atmosphere: Twenty-year mission will end. *Space Weather*, *10*(5), S05006. https://doi.org/10.1029/2012SW000804

Belakhovsky, V. B., Pilipenko, V. A., Antonova, E. E., Miyoshi, Y., Kasahara, Y., Kasahara, S., et al. (2023). Relativistic electron flux growth during storm and non-storm periods as observed by ARASE and GOES satellites. *Earth Planets and Space*, *75*(1), 189. https://doi.org/10.1186/s40623-023-01925-1

Blum, L., Li, X., & Denton, M. (2015). Rapid MeV electron precipitation as observed by SAMPEX/HILT during high-speed stream-driven storms. *Journal of Geophysical Research: Space Physics*, *120*(5), 3783–3794. https://doi.org/10.1002/2014JA020633

Brasseur, G., & Solomon, S. (2005). *Aeronomy of the middle atmosphere* (3rd ed.). D. Reidel.

Carpenter, D. L., & Anderson, R. R. (1992). An ISEE/whistler model of equatorial electron density in the magnetosphere. *Journal of Geophysical Research*, *97*(A2), 1097–1108. https://doi.org/10.1029/91JA01548

Cresswell-Moorcock, K., Rodger, C. J., Kero, A., Collier, A. B., Clilverd, M. A., Häggström, I., & Pitkänen, T. (2013). A reexamination of latitudinal limits of substorm-produced energetic electron precipitation. *Journal of Geophysical Research: Space Physics*, *118*(10), 6694–6705. https://doi.org/10.1002/jgra.50598

Cussac, T., Clair, M.-A., Pascale, U.-G., Buisson, F., Gerard, L.-B., Ledu, M., et al. (2006). The Demeter microsatellite and ground segment. *Planetary and Space Science*, *54*(5), 413–427. https://doi.org/10.1016/j.pss.2005.10.013

Dietrich, S., Rodger, C. J., Clilverd, M. A., Bortnik, J., & Raita, T. (2010). Relativistic microburst storm characteristics: Combined satellite and ground-based observations. *Journal of Geophysical Research*, *115*(A12), A12240. https://doi.org/10.1029/2010JA015777

Douma, E., Rodger, C. J., Blum, L. W., & Clilverd, M. A. (2017). Occurrence characteristics of relativistic electron microbursts from SAMPEX observations. *Journal of Geophysical Research: Space Physics*, *122*(8), 8096–8107. https://doi.org/10.1002/2017JA024067

Douma, E., Rodger, C. J., Blum, L. W., O'Brien, T. P., Clilverd, M. A., & Blake, J. B. (2019). Characteristics of relativistic microburst intensity from SAMPEX observations. *Journal of Geophysical Research: Space Physics*, *124*(7), 5627–5640. https://doi.org/10.1029/2019JA026757

Evans, D. S., & Greer, M. S. (2006). *Polar orbiting Environmental satellite space Environment Monitor–2 instrument descriptions and archive data documentation, NOAA Tech. Mem. 1.4, (SEM2v2.0.doc, rev 2006)*. Space Environ. Lab.

Forsyth, C., Rae, I. J., Coxon, J. C., Freeman, M. P., Jackman, C. M., Gjerloev, J., & Fazakerley, A. N. (2015). A new technique for determining substorm onsets and phases from indices of the electrojet (SOPHIE). *Journal of Geophysical Research: Space Physics*, *120*(12), 10592–10606. https://doi.org/10.1002/2015JA021343

Hendry, A. T., Rodger, C. J., & Clilverd, M. A. (2017). Evidence of sub-MeV EMIC-driven electron precipitation. *Geophysical Research Letters*, *44*(3), 1210–1218. https://doi.org/10.1002/2016GL071807

Jaynes, A. N., Baker, D. N., Singer, H. J., Rodriguez, J. V., Loto'aniu, T. M., Ali, A. F., et al. (2015). Source and seed populations for relativistic electrons: Their roles in radiation belt changes. *Journal of Geophysical Research: Space Physics*, *120*(9), 7240–7254. https://doi.org/10.1002/2015JA021234

Klecker, B., Hovestadt, D., Scholer, M., Arbinger, H., Ertl, M., Kastele, H., et al. (1993). Hilt: A heavy ion large area proportional counter telescope for solar and anomalous cosmic rays. *IEEE Transactions on Geoscience and Remote Sensing*, *31*(3), 542–548. https://doi.org/10.1109/36.225520

Macmillan, S., & Maus, S. (2005). International geomagnetic reference field—The tenth generation. *Earth Planet Sp*, *57*(12), 1135–1140. https://doi.org/10.1186/BF03351896

Matthes, K., Funke, B., Andersson, M. E., Barnard, L., Beer, J., Charbonneau, P., et al. (2017). Solar forcing for CMIP6 (v3.2). *Geoscience Modelling Development*, *10*(6), 2247–2302. https://doi.org/10.5194/gmd-10-2247-2017

Nakamura, R., Kamei, K., Kamide, Y., Baker, D. N., Blake, J. B., & Looper, M. (1998). SAMPEX observations of storm-associated electron flux variations in the outer radiation belt. *Journal of Geophysical Research*, *103*(A11), 26261–26269. https://doi.org/10.1029/97JA02873

Nesse Tyssøy, H., Partamies, N., Babu, E. M., Smith-Johnsen, C., & Salice, J. A. (2021). The predictive capabilities of the auroral electrojet index for medium energy electron precipitation. *Frontiers in Astronomy Space Science*, *8*, 714146. https://doi.org/10.3389/fspas.2021.714146

O'Brien, T. P., & Moldwin, M. B. (2003). Empirical plasmapause models from magnetic indices. *Geophysical Research Letters*, *30*(4), 1152. https://doi.org/10.1029/2002GL016007

Peck, E. D., Randall, C. E., Green, J. C., Rodriguez, J. V., & Rodger, C. J. (2015). POES MEPED differential flux retrievals and electron channel contamination correction. *Journal of Geophysical Research: Space Physics*, *120*(6), 4596–4612. https://doi.org/10.1002/2014JA020817

Ripoll, J.-F., Claudepierre, S. G., Ukhorskiy, A. Y., Colpitts, C., Li, X., Fennell, J., & Crabtree, C. (2020). Particle dynamics in the Earth's radiation belts: Review of current research and open questions. *Journal of Geophysical Research: Space Physics*, *125*(5), e2019JA026735. https://doi.org/10.1029/2019JA026735

Rodger, C. J., Carson, B. R., Cummer, S. A., Gamble, R. J., Clilverd, M. A., Green, J. C., et al. (2010). Contrasting the efficiency of radiation belt losses caused by ducted and nonducted whistler-mode waves from ground-based transmitters. *Journal of Geophysical Research*, *115*(A12), A12208. https://doi.org/10.1029/2010JA015880

Rodger, C. J., Clilverd, M. A., Green, J. C., & Lam, M. M. (2010). Use of POES SEM-2 observations to examine radiation belt dynamics and energetic electron precipitation into the atmosphere. *Journal of Geophysical Research*, *115*(A4), A04202. https://doi.org/10.1029/2008JA014023

Rodger, C. J., Clilverd, M. A., Hendry, A. T., & Forsyth, C. (2022). Examination of radiation belt dynamics during substorm clusters: Magnetic local time variation and intensity of precipitating fluxes. *Journal of Geophysical Research: Space Physics*, *127*(12), e2022JA030750. https://doi.org/10.1029/2022JA030750

Rodger, C. J., Cresswell-Moorcock, K., & Clilverd, M. A. (2016). Nature's Grand Experiment: Linkage between magnetospheric convection and the radiation belts. *Journal of Geophysical Research: Space Physics*, *121*(1), 171–189. https://doi.org/10.1002/2015JA021537

Sauvaud, J.-A., Moreau, T., Maggiolo, R., Treilhou, J., Jacquey, C., Cros, A., et al. (2006a). High-energy electron detection onboard DEMETER: The IDP spectrometer, description and first results on the inner belt. *PSS*, *54*(5), 502–511. https://doi.org/10.1016/j.pss.2005.10.019

Shprits, Y. Y., Meredith, N. P., & Thorne, R. M. (2007). Parameterization of radiation belt electron loss time scales due to interaction with chorus waves. *Geophysical Research Letters*, *34*(11), L11110. https://doi.org/10.1029/2006GL029050

Simms, L., Engebretson, M., Clilverd, M., Rodger, C., Lessard, M., Gjerloev, J., & Reeves, G. (2018). A distributed lag autoregressive model of geostationary relativistic electron fluxes: Comparing the influences of waves, seed and source electrons, and solar wind inputs. *Journal of Geophysical Research: Space Physics*, *123*(5), 3646–3671. https://doi.org/10.1029/2017JA025002

Thomsen, M. F. (2004). Why Kp is such a good measure of magnetospheric convection. *Space Weather*, *2*(11), S11004. https://doi.org/10.1029/2004SW000089

Usanova, M. E., Drozdov, A., Orlova, K., Mann, I. R., Shprits, Y., Robertson, M. T., et al. (2014). Effect of EMIC waves on relativistic and ultra relativistic electron populations: Ground-based and Van Allen Probes observations. *Geophysical Research Letters*, *41*(5), 1375–1381. https://doi.org/10.1002/2013GL059024

Van De Kamp, M., Seppälä, A., Clilverd, M. A., Rodger, C. J., Verronen, P. T., & Whittaker, I. C. (2016). A model providing long-term data sets of energetic electron precipitation during geomagnetic storms. *Journal of Geophysical Research Atmoshere*, *121*, 12520–12540. https://doi.org/10.1002/2015JD024212

Whittaker, I. C., Clilverd, M. A., & Rodger, C. J. (2014). Characteristics of precipitating energetic electron fluxes relative to the plasmapause during geomagnetic storms. *Journal of Geophysical Research: Space Physics*, *119*(11), 8784–8800. https://doi.org/10.1002/2014JA020446

Whittaker, I. C., Gamble, R. J., Rodger, C. J., Clilverd, M. A., & Sauvaud, J.-A. (2013). Determining the spectra of radiation belt electron losses: Fitting DEMETER electron flux observations for typical and storm times. *Journal of Geophysical Research: Space Physics*, *118*(12), 7611–7623. https://doi.org/10.1002/2013JA019228

Yando, K., Millan, R. M., Green, J. C., & Evans, D. S. (2011). A Monte Carlo simulation of the NOAA POES medium energy proton and electron detector instrument. *Journal of Geophysical Research*, *116*(A10), A10231. https://doi.org/10.1029/2011JA016671

Zhao, H., & Li, X. (2013). Inward shift of outer radiation belt electrons as a function of Dst index and the influence of the solar wind on electron injections into the slot region. *Journal of Geophysical Research: Space Physics*, *118*(2), 756–764. https://doi.org/10.1029/2012JA018179